Journal of Alloys and Compounds 509 (2011) 5408–5413

Contents lists available at ScienceDirect

Journal of Alloys and Compounds

journal homepage: www.elsevier.com/locate/jallcom

Synthesis of carbon coated nanocrystalline porous α-$LiFeO_2$ composite and its application as anode for the lithium ion battery

M.M. Rahman[a,b,*], Jia-Zhao Wang[a,b], Mohd Faiz Hassan[a,b,c], Zhixin Chen[d], Hua-Kun Liu[a,b]

[a] Institute for Superconducting and Electronic Materials, University of Wollongong, NSW 2522, Australia
[b] ARC Centre of Excellence for Electromaterials Science, University of Wollongong, NSW 2522, Australia
[c] Department of Science Physics, University of Malaysia Terengganu, Kuala Terengganu 20522, Malaysia
[d] School of Mechanical, Materials and Mechatronic Engineering, University of Wollongong, NSW 2522, Australia

ARTICLE INFO

Article history:
Received 11 January 2011
Received in revised form 11 February 2011
Accepted 11 February 2011
Available online 21 February 2011

Keywords:
Li-ion battery
α-$LiFeO_2$-C nanocomposite
Molten salt
Porous architecture

ABSTRACT

In this work, we describe for the first time a high surface area nanocrystalline porous α-$LiFeO_2$-C composite anode material synthesized by a simple molten salt method, followed by a carbon coating process. The synthesized nanocomposite presents an interconnected porous architecture, as was confirmed by field emission scanning electron microscope observations. Transmission electron microscope investigations revealed that amorphous carbon was incorporated into the pores among the nanoparticles and that some nanoparticles were covered by a thin layer of amorphous carbon as well. Electrochemical measurements showed that the carbon played an important role, as it affected both the cycle life and the rate capability of the electrode. The α-$LiFeO_2$-C nanocomposite electrode delivered a higher reversible capacity and good cycle stability (540 mAh g^{-1} at 1 C after 200 cycles) compared to the pure α-$LiFeO_2$ electrode. Good electrochemical performance of the α-$LiFeO_2$-C nanocomposite electrode could be attributed to the porous conductive architecture among the nanoparticles, which not only has benefits in terms of decreasing the absolute volume changes and increasing the mobility of lithium ions, but also offers conductive pathways along the whole interconnected wall in the structure, which is favourable for the transport of electrons, promotes liquid electrolyte diffusion into the bulk material, and acts as a buffer zone to absorb the volume changes. Our results indicate that α-$LiFeO_2$-C nanocomposite could be considered as a potential anode material for lithium-ion batteries.

1. Introduction

In order to address power and energy demands of mobile electronics and electric cars, Li-ion technology is urgently being optimized by using alternative materials [1]. High-performance lithium ion batteries must satisfy stringent requirements, including large reversible capacity, high rate capability, and long-term cycle life, with solutions to these requirements lying mainly in advanced materials [2,3]. Among all the materials applicable for Li-ion battery anodes, transition metal oxides have always been regarded as the most promising candidates due to their relatively lower cost, environmental benignity, higher theoretical capacity, and better safety during operation compared to other materials [4–6]. Due to the low theoretical capacity (372 mAh g^{-1}) of graphitic carbon, which is the most commonly used anode material, intensive research has been conducted to search for alternative anode materials with higher capacities and rate capabilities [7–9]. Traditional Li-storage materials suffer serious capacity loss when charged and discharged at high rates, which is mainly due to large polarization and slow diffusion of lithium ions and electrons in the active materials [10]. Adopting electrode materials with fine nanoparticles, hollow/porous architecture, and tunable morphology has been attempted to solve these problems. The main reason is that their nanocrystalline porous architectures present large surface areas and thin walls, which are beneficial to the transportation of lithium ions in the active materials and to decreased polarization [10–17]. However, among all the transition metal oxides, iron oxide has attracted much attention because it is non-toxic and contains the most abundant and low cost metal available in the world [18–22]. It is well known that $LiFeO_2$ has different forms, i.e., α, β, and γ-conjugated forms, as determined by the method and conditions of synthesis, and the various forms were also studied as potential alternatives to Li–Co–O positive electrodes [23–28]. In terms of use as a cathode material, many problems still remain, such as a low operating voltage, poor electrochemical activity, especially for the cubic α and γ-forms, and low capacity retention during the cycling tests. Despite its poor electrochemical characteristics as a cathode in lithium-ion bat-

* Corresponding author at: Institute for Superconducting and Electronic Materials, University of Wollongong, NSW 2522, Australia. Tel.: +61 242981471; fax: +61 242215731.
E-mail addresses: mmr543@uow.edu.au, mokhles_utm@yahoo.com (M.M. Rahman).

0925-8388/$ – see front matter © 2011 Elsevier B.V. All rights reserved.
doi:10.1016/j.jallcom.2011.02.067

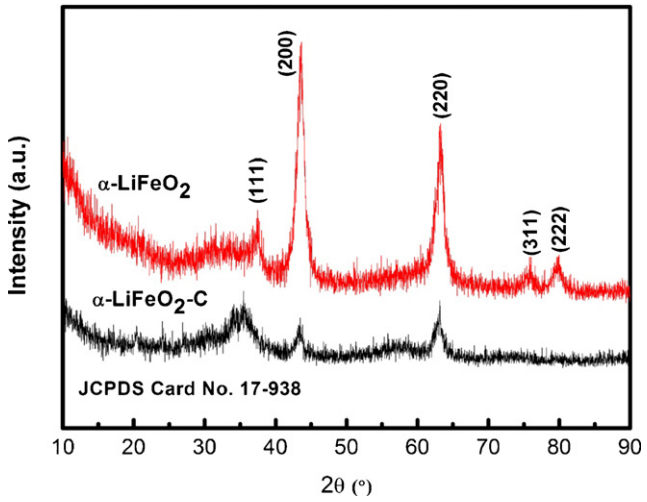

Fig. 1. X-ray diffraction patterns of α-$LiFeO_2$ and α-$LiFeO_2$-C nanocomposite.

teries, $LiFeO_2$ has been investigated as an anode material within the voltage range of 0.01–2.5 V vs. Li/Li^+ [19]. Yet until now, there have been very few reports on $LiFeO_2$ materials used as anode for the Li-ion batteries. Unfortunately, none of the reported results shows promising anode properties in rechargeable lithium cells [19,29]. So, it is very interesting to explore the synthesis of α-$LiFeO_2$ materials (theoretical specific capacity 848 mAh g^{-1}) and their application as anode for the Li-ion battery. It is still a great challenge to improve the cycling stability and high rate capability of iron-based materials. In particular, the rate capability in a lithium-ion battery system is limited by the transportation of both lithium ions and electrons [7,30,31]. By depositing nanostructured materials into/onto a conducting matrix (metal or carbon), the high rate capability was significantly improved [30,32]. Different conductive fillers have been extensively explored for composite components and significant improvement in electrical conductivity arising from the increase of filler content was observed for most composites and it was explained by the percolation transition of the conductive network formation [33,34]. However, carbon coating is one of the most widely used surface modification techniques, and in fact, carbon is very stable anode materials in lithium-ion batteries due to the small volume change during Li insertion/extraction [35]. The solid electrolyte interphase (SEI) films on the carbon surface are also relatively stable, and the carbon coating may serve as a perfect barrier to protect the inner active materials and maintain their high capacities [36–38]. Furthermore, a selected binder, sodium carboxymethyl cellulose (CMC), can also improve the cycling performance of iron-based materials [11,39].

Herein, this is the first time that the synthesis of nanocrystalline porous α-$LiFeO_2$-C composite by a simple molten salt method, followed by a carbon coating process, has been reported, and its application as anode for the Li-ion battery, with significant improvement of capacity retention and rate capability, is also discussed.

2. Experimental

The α-$LiFeO_2$ powder was synthesized by mixing together $FeCl_2{\cdot}4H_2O$ (Aldrich, 95%), $LiOH{\cdot}H_2O$ (Sigma-Aldrich, 98%), $LiNO_3$ (Sigma-Aldrich, 99.9%), and Li_2O_2 (Sigma-Aldrich, 90%) with a molar ratio of 0.01:0.1:0.1:0.01, and the mixture was ground in a mortar with a pestle until it became homogeneous. The powder mixture was vacuum dried at 120 °C for 24 h. The drying process was used to minimize the water content in the starting material mixture for the molten salt process ($LiNO_3$–$LiOH.H_2O$). The mixture was immediately placed in an alumina crucible, and heated to and kept at 300 °C for 3 h in a muffle furnace in air. At this tempera-

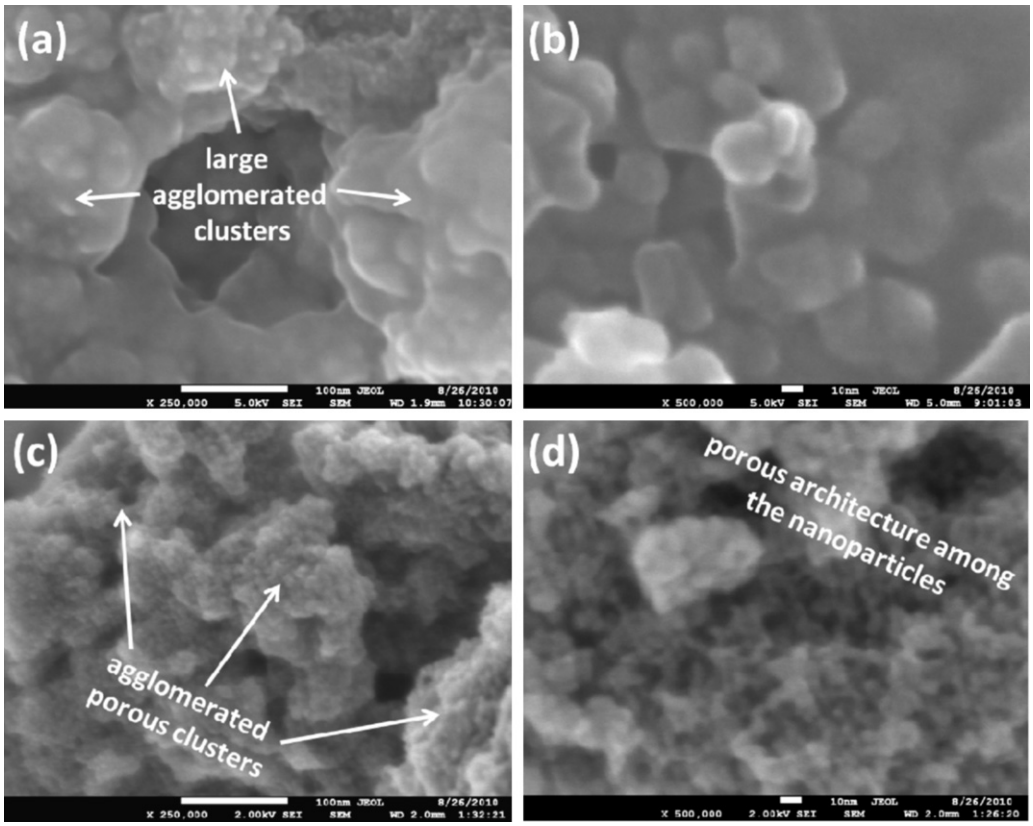

Fig. 2. FE-SEM images of α-$LiFeO_2$ and α-$LiFeO_2$-C powder samples: (a) low magnification image of the agglomerated clusters of α-$LiFeO_2$; (b) high magnification image of a cluster of α-$LiFeO_2$ composed of numerous nanoparticles; (c) low magnification image of α-$LiFeO_2$-C composite, consisting of numerous agglomerated tiny particles; (d) high-resolution image of α-$LiFeO_2$-C composite, which exhibits a porous conductive architecture among the nanoparticles.

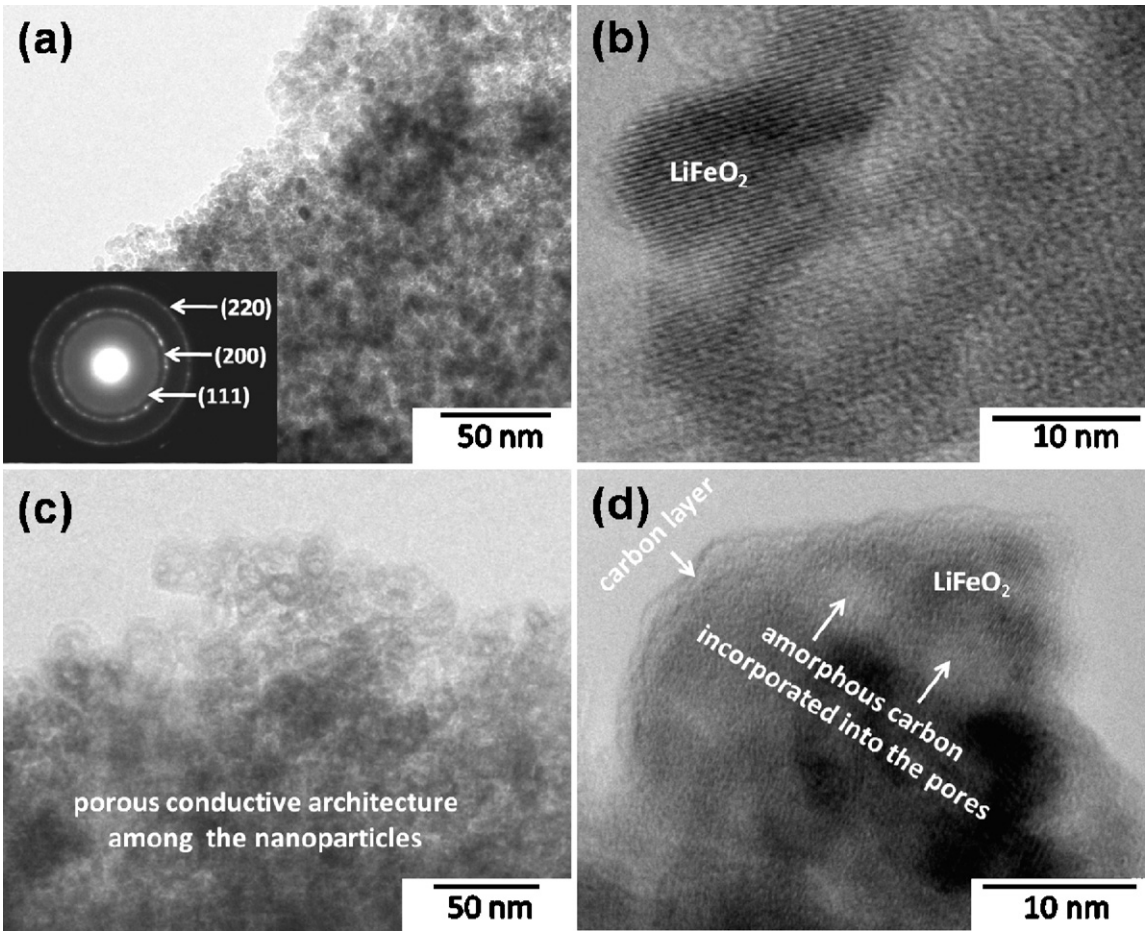

Fig. 3. (a) TEM image with its corresponding SAED pattern (inset) and (b) HRTEM image of the α-$LiFeO_2$ sample; (c) TEM and (d) HRTEM images of the α-$LiFeO_2$-C sample.

ture, the $LiNO_3$:$LiOH{\cdot}H_2O$:Li_2O_2 mixture was melted to become a molten salt near the eutectic composition. This is significantly different from an aqueous solution, and the water content in the molten salt solution was reduced as much as possible. The resulting products were washed with large amounts of ethanol and distilled water, followed by drying at 100 °C for 12 h under a vacuum pressure of 0.1 MPa. The synthesized α-$LiFeO_2$ nanoparticles were then coated with amorphous carbon. Toluene (C_7H_8, 99.5%) and malic acid ($C_4H_6O_5$, 99%) were used as a solvent and a carbon source during the coating process, respectively. The amount of carbon content in the composite depends on the amount of malic acid used. Different amount of carbon containing composites can be achieved using different amount of malic acid. The ratio of malic acid and active material (α-$LiFe_2O_2$) was maintained 1:1 in our system. In this instance, malic acid ($C_4H_6O_5$) was chosen as the carbon source, due to its low decomposition temperature (150 °C) and low oxygen content compared to other common carbon sources such as citric acid ($C_6H_8O_7$), sucrose ($C_{12}H_{22}O_{11}$), and glucose ($C_6H_{12}O_6$), etc. Both α-$LiFeO_2$ and malic acid were dispersed together in toluene with continuous stirring at room temperature for 2 h. The slurry was dried at 100 °C for 6 h at a vacuum pressure of 0.1 MPa and then further heat-treated at 300 °C for 3 h in air atmosphere. The resultant particles were collected, washed, and vacuum treated again at 120 °C for 24 h to eliminate residual water on the particle surfaces.

X-ray diffraction (XRD) data were collected from powder samples on a GBC MMA diffractometer (with Cu Kα radiation and a graphite monochromator) at a scanning rate of 2° min^{-1} for 2θ in the range of 10–90°. Traces™ software in combination with the Joint Committee on Powder Diffraction Standards (JCPDS) powder diffraction files was used to identify the phases present. Raman analysis was performed using a Raman spectrometer (Jobin Yvon HR800). The amount of amorphous carbon in the composite sample was estimated using a Mettler-Toledo thermogravimetric analysis/differential scanning calorimetry (TGA/DSC) 1 Star^e System from 50 to 800 °C at 5 °C min^{-1}. The Brunauer–Emmett–Teller (BET) surface area of the synthesized materials was measured by a NOVA 1000 high speed gas sorption analyzer (Quantachrome Corporation, USA). The morphologies of the samples were investigated by field emission scanning electron microscopy (FE-SEM; JEOL JSM-7500FA) and transmission electron microscopy (TEM) using a JEOL 2011 analytical electron microscope equipped with a JEOL energy dispersive X-ray spectroscopy (EDS) system. TEM samples were prepared by deposition of ground particles onto holey carbon support films, with care taken to ensure that selected area electron diffraction (SAED) and high resolution TEM contrast were obtained only from sample regions located over holes in the holey carbon support films. To test the electrochemical performance, sample powders were mixed with acetylene black (AB) and a binder, carboxymethyl cellulose (CMC), in a weight ratio of 80:15:5 in a solvent (distilled water). The slurry was spread onto copper foil substrates. The coated electrodes were dried in a vacuum oven at 110 °C for 24 h to remove water molecules. The electrode was then pressed using a disc with a diameter of 14 mm to enhance the contact between the copper foil, active materials, and conductive carbon. Subsequently, the electrodes were cut to a 1 cm × 1 cm size. CR 2032 coin-type cells were assembled in an Ar-filled glove box (Mbraun, Unilab, Germany) using lithium metal foil as the counter electrode. The electrolyte was 1 M $LiPF_6$ in a mixture of ethylene carbonate (EC) and dimethyl carbonate (DMC) (1:1 by volume, provided by MERCK KgaA, Germany). The cells were galvanostatically discharged and charged in the range of 0.01–2.5 V. Cyclic voltammograms of the electrodes were collected with a scan rate of 0.1 mV/s between 0.01 and 2.5 V vs. Li/Li^+.

3. Results and discussion

The XRD patterns of the resulting products with and without carbon coating are shown in Fig. 1. These patterns exhibited several peaks that could be ascribed to α-$LiFeO_2$ and were indexed in the cubic system with lattice parameter a = 4.158 Å, which is quite consistent with the reported value (JCPDS 17-938). The carbon-coated sample shows a decrease in the intensity of the main peaks with a shift of (1 1 1). Since the heat-treatment temperature is low, it is proposed that the coated carbon is amorphous and that the amorphous carbon coating on the surface is responsible for the weakening of the intensities of the XRD peaks [40]. However, amorphous carbon in the composite product was experimentally detected by Raman spectroscopy (Fig. S1, Supporting information) [41]. An additional small and broad peak at ~30° may be due to the presence of amorphous phase as the synthesis method is con-

ducted at relatively low temperature. The approximate crystallite sizes of the α-$LiFeO_2$ and α-$LiFeO_2$-C powder samples were calculated using the Debye–Scherrer equation applied to the marked peaks, assumed to be originating from (2 2 0), and the crystal sizes were 6.45 nm and 5.42 nm, respectively. The specific surface areas were also measured to be 97.98 $m^2\,g^{-1}$ for the α-$LiFeO_2$ and 115.52 $m^2\,g^{-1}$ for the α-$LiFeO_2$-C by the 15 BET N_2 adsorption method. To estimate the amount of amorphous carbon in the α-$LiFeO_2$-C composite materials, TGA was carried out in air (Fig. S2, Supporting information). The samples were heated from 50 to 800 °C at a rate of 5 °C min^{-1}. As the α-$LiFeO_2$ powders remained stable over the selected temperature range, any weight change is believed to correspond to the oxidation of amorphous carbon [42]. It was estimated that the amount of total weight loss in the composite was approximately 25 wt.%, where ~6 wt.% weight loss could be considered as from loss of moisture and volatile organic compounds in the α-$LiFeO_2$-C, starting from 50 °C. The remaining amount, ~19 wt.%, was attributed to the amorphous carbon produced by the decomposition of malic acid ($C_4H_6O_5$) in the precursor.

Field emission scanning electron microscope (FE-SEM) images of the α-$LiFeO_2$ and α-$LiFeO_2$-C powder samples are shown in Fig. 2. A low magnification FE-SEM image of α-$LiFeO_2$ (Fig. 2(a)) shows that the sample consists of large agglomerated clusters. When scanned under high magnification, it can be seen that each cluster is composed of numerous spherical nanoparticles, each having a smooth surface and a typical diameter of ~10–20 nm (Fig. 2(b)). A very interesting morphological change is observed when the sample is coated with amorphous carbon. In the case of α-$LiFeO_2$-C, a low magnification image (Fig. 2(c)) demonstrates that the sample consists of numerous agglomerated porous nanoclusters. These nanoclusters are composed of very tiny nanoparticles, with a porous architecture among the nanoparticles clearly seen under high magnification (Fig. 2(d)), which can account for the high surface area of the α-$LiFeO_2$-C sample. The formation mechanism of such a porous conductive architecture is not clearly understood yet, however, there is a possible explanation: toluene and malic acid were used as the solvent and the carbon source during the coating process, respectively. Both α-$LiFeO_2$ and malic acid were dispersed together in toluene with continuous stirring. The mixture was dried at 100 °C for 6 h at a vacuum pressure of 0.1 MPa to eliminate toluene from the mixture, and thus, malic acid was trapped among the α-$LiFeO_2$ particles. Due to the further heat-treatment at 300 °C, α-$LiFeO_2$ particles were agglomerated, and at the same time, malic acid was decomposed, which produces amorphous carbon, CO_2, water vapour and energy (see Eq. (1)). CO_2, water vapour and energy could contribute together to penetrate the agglomerated clusters and, upon being released, leave pores behind, thus generating the porous conductive architecture among the nanoparticles.

$$\alpha\text{-}LiFeO_2 + C_4H_6O_5 \rightarrow \alpha\text{-}LiFeO_2/C + CO_2\uparrow + H_2O\uparrow + \text{energy}\uparrow \quad (1)$$

However, to verify the formation of the α-$LiFeO_2$-C nanocomposite, EDS mapping analysis was used, as shown in Fig. S3, Supporting information, where the bright spots correspond to the presence of the elements Fe, O, and C, respectively.

TEM investigations further revealed that the samples consist of tiny particles with a spheroidal shape range in size from ~10–20 nm for the α-$LiFeO_2$ and ~5–10 nm for the α-$LiFeO_2$-C nanocomposite, respectively. Fig. 3(a) shows a low magnification image and the corresponding selected area electron diffraction (SAED) pattern (inset) of the α-$LiFeO_2$ sample, where all of the ring spots were evaluated to represent *d*-spacings of 0.24, 0.20, and 0.14 nm, which can be referred to the crystallographic directions of (1 1 1), (2 0 0), and (2 2 0), respectively. These results are also consistent with the standard information provided by the XRD patterns. Fig. 3(b) presents

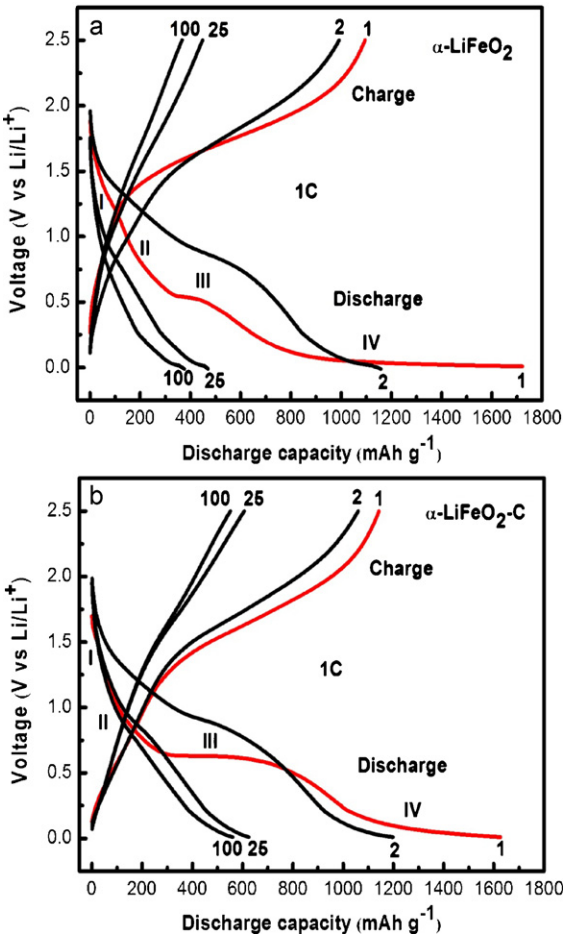

Fig. 4. Typical charge–discharge curves of α-$LiFeO_2$ electrode (a) and α-$LiFeO_2$-C nanocomposite electrode (b) for selected cycles at 1 C (848 mAh g^{-1}) in the voltage range of 0.01–2.5 V.

a high resolution TEM (HRTEM) image of the same sample, and the lattice fringes of $LiFeO_2$ crystals are visible. On the other hand, amorphous carbon incorporated into the pores is clearly observed among the nanoparticles of the α-$LiFeO_2$-C sample (Fig. 3(c)). High resolution imaging of the C-containing sample (Fig. 3(d)) also resulted in contrast consistent with the presence of carbon incorporated into pores among the nanocrystals, and some nanocrystals are covered by a thin layer of carbon, as well.

The galvanostatic charge–discharge curves for the 1st, 2nd, 25th, and 100th cycles of α-$LiFeO_2$ and α-$LiFeO_2$-C composite electrodes cycled between 0.01 and 2.5 V are shown in Fig. 4. During the first cycle the lithium insertion proceeds through different steps, and the first discharge curves can be divided into four regions, marked as I, II, III, and IV. From regions I to III, the theoretical capacity of α-$LiFeO_2$ could be calculated on the basis of the following electrochemical reaction [19]:

$$\alpha\text{-}LiFeO_2 + 3Li \rightarrow Fe + 2LiO_2 \quad (2)$$

where $3e^-$ shift from Li^0 to α-$LiFeO_2$, and the reduction reaction of Fe (III) to Fe (0) takes place with a theoretical capacity of 848 mAh g^{-1}, corresponding to a maximum lithium uptake of 3 Li per α-$LiFeO_2$. The initial discharge capacities were measured to be 1722 mAh g^{-1} for the α-$LiFeO_2$ electrode and 1626 mAh g^{-1} for the α-$LiFeO_2$-C electrode, respectively. For the following several cycles, capacities were higher than the theoretical capacity for both electrodes. The extra capacity (region IV) could be explained by the decomposition of electrolyte to form the solid electrolyte interphase (SEI) layer [43] or by further lithium storage via interfa-

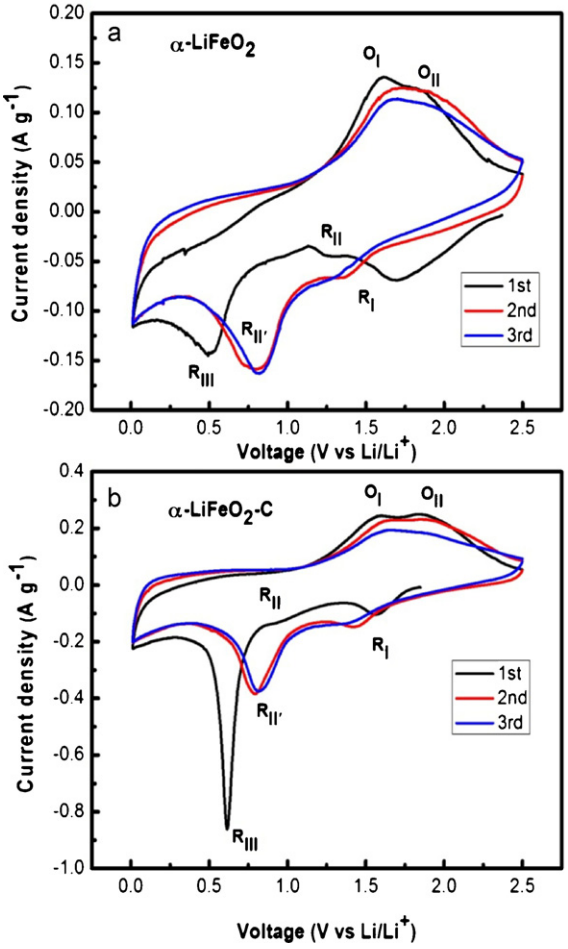

Fig. 5. Typical cyclic voltammograms of α-$LiFeO_2$ electrode (a) and α-$LiFeO_2$-C nanocomposite electrode (b) for selected cycles with a scan rate of 0.1 mV s^{-1} between 0.01 and 2.5 V.

cial reaction due to the charge separation at the metal/Li_2O phase boundary [44]. It should be noted that the α-$LiFeO_2$-C nanocomposite electrode can maintain a reversible capacity of around 560 mAh g^{-1} for 100 cycles, while the α-$LiFeO_2$ gradually loses its reversible capacity down to approximately 374 mAh g^{-1} over 100 cycles. However, the initial irreversible behaviour and the capacity fading observed for the materials have to be associated with this irreversible reduction. To further investigate the electrochemical behaviour, cyclic voltammetry (CV) (Fig. 5) measurements were carried out with a scan rate of 0.1 mV s^{-1}. The initial cathodic scan results in mainly three peaks (R_I, R_{II}, and R_{III}), which correspond to regions I, II, and III. After the first cycle, the reduction peak consists of a main peak in the form of one broad peak ($R_{II'}$). The electrode activation via the 1st cycle and the strongly overlapping trend of the subsequent cycles indicate that electrochemical reversibility has set in after the initial cycle. The positive scan shows two peaks (O_I at 1.6 V and O_{II} at 1.8 V). The O_I and O_{II} peaks correspond to the oxidation reactions of Fe(0)/Fe(II) and Fe(II)/Fe(III), respectively [45]. The good reversibility of the reaction from Fe(0) to Fe(III) is observed for the α-$LiFeO_2$-C electrode, while there is no transformation from Fe(II) to Fe(III) in the subsequent cycles for the α-$LiFeO_2$ electrode. In addition, the cathodic peak at around 0.51 V for the α-$LiFeO_2$ electrode and at around 0.63 V for the α-$LiFeO_2$-C electrode match well with the first discharge voltage plateau, as shown in Fig. 4(a) and (b). The cycling performance of both electrodes was investigated for up to 200 cycles at the 1 C rate, and the results are given in Fig. 6. The α-$LiFeO_2$-C nanocomposite electrode demonstrates a stable capacity as high as 540 mAh g^{-1}, even after 200 cycles, and only 4% capacity fading is observed from 50 to 200 cycles. For the α-$LiFeO_2$ electrode, there is significant degradation in the specific discharge capacity, which can be observed throughout the whole cycling process. The discharge capacity was measured to be only 349 mAh g^{-1} after 200 cycles. It should also be noted that 11% capacity fading is observed for the α-$LiFeO_2$ electrode from 50 to 200 cycles. Such a big difference in the electrochemical performance implies that the electrochemical properties of the α-$LiFeO_2$ electrode are greatly influenced by the carbon coating, which makes the materials more promising for further investigation for lithium-ion battery applications. Furthermore, the cycling performance of the α-$LiFeO_2$ and α-$LiFeO_2$-C nanocomposite electrodes at different charge/discharge rates, measured from 0.05 C to 2 C in an ascending order, followed by a return to 0.05 C, is shown in Fig. 7. The α-$LiFeO_2$-C nanocomposite electrode presents good cycling stability at each rate, and reversible capacities were measured to be 898, 747, 623, 505, 378, and 272 mAh g^{-1} at the rate of 0.05, 0.1, 0.2, 0.5, 1, and 2 C, respectively. After 50 cycles, the reversible capacity of the α-$LiFeO_2$-C nanocomposite electrode at 0.05 C was still 740 mAh g^{-1}, illustrating its good cycling performance, clearly much better than the performance of the α-$LiFeO_2$ electrode (397 mAh g^{-1}), even after cycling at high rates.

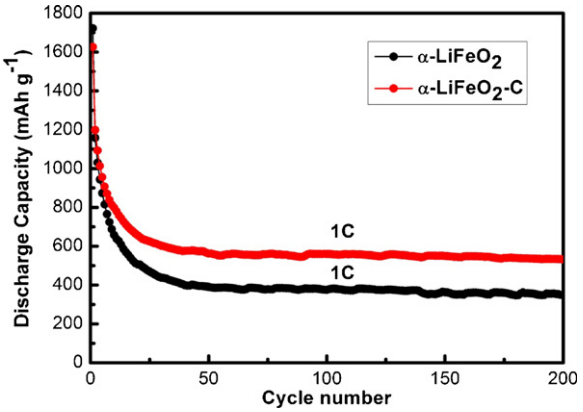

Fig. 6. Cycling stability of α-$LiFeO_2$ and α-$LiFeO_2$-C nanocomposite electrodes at 1 C (848 mAh g^{-1}) in the voltage range of 0.01–2.5 V.

In brief, several reasons could be given for the good electrochemical performance of the α-$LiFeO_2$-C nanocomposite electrode. The porous nanostructured α-$LiFeO_2$-C composite could provide better contact between the electrode and electrolyte, reducing the traverse time for both electrons and lithium ions. This also offers flexibility and toughness to absorb the contraction and

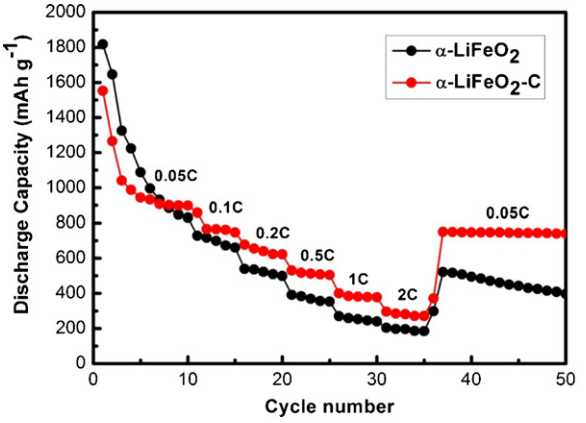

Fig. 7. Consecutive cycling behaviour of α-$LiFeO_2$ and α-$LiFeO_2$-C nanocomposite electrodes at different rates.

expansion during lithium-ion insertion/extraction, which would help to enhance the electrochemical performance [12,46–49]. On the other hand, carbon incorporated into the pores among the nanoparticles and the carbon coating around the nanocrystals, which could further extend the surface area and provide the carbon shell on the surface of the α-$LiFeO_2$ nanoparticles, are also beneficial for the electrolyte diffusion into the bulk of the anode, provide fast transport channels for the Li ions, and accommodate the volume variation more effectively, thus increasing the structural stability of the electrode and protecting the film from further high volume expansion during cycling [50,51]. So, it is believed that the carbon incorporated into the porous conductive architecture among the nanoparticles not only has benefits in terms of decreasing the absolute volume changes and the mobility of the lithium ions, but also offers a conductive pathway along the whole interconnected wall in the structure, which is favourable for the transport of electrons, promotes liquid electrolyte diffusion into the bulk material, and acts as a protective layer during the redox reaction.

4. Conclusions

In summary, our facile method consists of synthesizing a carbon coated nanocrystalline porous α-$LiFeO_2$-C composite by using the molten salt method followed by a carbon coating process, where malic acid provides a conductive network and carbon source as well. This conductive network in combination with the carbon incorporated into the nanopores was confirmed by FE-SEM and TEM observations. For comparison, nanocrystalline α-$LiFeO_2$ was also investigated. The α-$LiFeO_2$-C nanocomposite electrode delivered a higher reversible capacity and more stable cycle life compared to α-$LiFeO_2$ electrode. The high electrochemical performance can be ascribed to the novel, high-surface-area, carbon incorporated, porous conductive architecture, which can facilitate the contact between active materials and the electrolyte, enhance lithium and electron transport, and accommodate the volume variation during cycling. This work provides a simple and feasible platform for further advances in carbon-based nanoporous composites for different applications.

Acknowledgements

The authors are grateful for funding from the Australian Research Council (ARC) under an ARC Centre of Excellence Program (CE0561616) and an ARC Discovery project (DP0987805). The authors also thank Dr. T. Silver for critical reading of the manuscript.

Appendix A. Supplementary data

Supplementary data associated with this article can be found, in the online version, at doi:10.1016/j.jallcom.2011.02.067.

References

[1] H. Li, Z. Wang, Li. Chen, X. Huang, Adv. Mater. 21 (2009) 4593–4607.
[2] H. Ma, S. Zhang, W. Ji, Z. Tao, J. Chen, J. Am. Chem. Soc. 130 (2008) 5361–5367.
[3] D.W. Kim, Y.D. Ko, J.G. Park, B.K. Kim, Angew. Chem. Int. Ed. 46 (2007) 6654–6657.
[4] Y. Yu, L. Gu, C.L. Wang, A. Dhanabalan, P.A. Van Aken, J. Maier, Angew. Chem. Int. Ed. 48 (2009) 6485–6489.
[5] A.L.M. Reddy, M. Shaijumon, S.R. Gowda, P.M. Ajayan, Nano Lett. 9 (2009) 1002–1006.
[6] M.S. Park, G.X. Wang, Y.M. Kang, D. Wexler, S.X. Dou, H.K. Liu, Angew. Chem. Int. Ed. 46 (2007) 750–753.
[7] P.G. Bruce, B. Scrosati, J.M. Tarascon, Angew. Chem. Int. Ed. 47 (2008) 2930–2946.
[8] J. Chen, F. Cheng, Acc. Chem. Res. 42 (2009) 713–723.
[9] D. Larcher, S. Beattie, M. Morcrette, K. Edstroem, J.C. Jumas, J.M Tarascon, J. Mater. Chem. 17 (2007) 3759–3772.
[10] H.W. Yan, S. Sokolov, J.C. Lytle, A. Stein, F. Zhang, W.H. Smyrl, J. Electrochem. Soc. 150 (2003) A1102–A1107.
[11] S.L. Chou, J.Z. Wang, D. Wexler, K. Konstantinov, C. Zhong, H.K. Liu, S.X. Dou, J. Mater. Chem. 20 (2010) 2092–2098.
[12] Z.P. Guo, G.D. Du, Y. Nuli, M.F. Hassan, H.K. Liu, J. Mater. Chem. 19 (2009) 3253–3257.
[13] H. Yamada, T. Yamato, I. Moriguchi, T. Kudo, Chem. Lett. 33 (2004) 1548.
[14] J.C. Lytle, H.W. Yan, N.S. Ergang, W.H. Smyrl, A. Stein, J. Mater. Chem. 14 (2004) 1616–1622.
[15] J.S. Sakamoto, B. Dunn, J. Mater. Chem. 12 (2002) 2859–2871.
[16] Z. Bing, Y. Yuan, Y. Wang, Z.W. Fu, Electrochem. Solid-State Lett. 9 (2006) A101–A104.
[17] L.J. Fu, T. Zhang, Q. Cao, H.P. Zhang, Y.P. Wu, Electrochem. Commun. 9 (2007) 2140–2144.
[18] W.F. Bin, C. Jie, H.K. Long, L.S. Qin, Sci. China Ser. E: Tech. Sci. 52 (11) (2009) 3219–3223.
[19] S. Uzunova, I. Uzunova, D. Kovacheva, A. Momchilov, B. Puresheva, J. Appl. Electrochem. 36 (2006) 1333–1339.
[20] Y.S. Lee, C.S. Yoon, Y.K. Sun, K. Kobayakawa, Y. Sato, Electrochem. Commun. 4 (2002) 727–731.
[21] G.Y. Zhang, Y.Y. Xu, D.Z. Gao, Y.Q. Sun, J. Alloys Compd. 509 (2011) 885–890.
[22] X.L. Xie, H.Q. Yang, F.H. Zhang, L. Li, J.H. Ma, H. Jiao, J.Y. Zhang, J. Alloys Compd. 477 (2009) 90–99.
[23] R. Kanno, T. Shirane, Y. Inaba, Y. Kawamoto, J. Power Sources 68 (1997) 145–152.
[24] Y. Sakurai, H. Arai, S. Okada, J. Yamaki, J. Power Sources 68 (1997) 711–715.
[25] Y. Sakurai, H. Arai, Y. Yamaki, Solid State Ionics 113–115 (1998) 29–34.
[26] T. Matsumura, R. Kanno, Y. Inaba, Y. Kawamoto, M. Takano, J. Electrochem. Soc. 149 (2002) A1509–1513.
[27] X. Wang, L. Gao, F. Zhou, Z. Zhang, M. Ji, C. Tang, T. Shen, H. Zheng, J. Cryst Growth 265 (2004) 220–223.
[28] J. Morales, J. Santos-Pena, Electrochem. Commun. 9 (2007) 2116–2120.
[29] P.P. Prosini, M. Carewska, S. Loreti, C. Minarini, S. Passerini, Int. J. Inorg. Mater. 2 (2000) 365–370.
[30] P.L. Taberna, S. Mitra, P. Poizot, P. Simon, J.M. Tarascon, Nat. Mater. 5 (2006) 567–573.
[31] Y.G. Guo, J.S. Hu, L.J. Wan, Adv. Mater. 20 (2008) 2878–2887.
[32] Y.G. Guo, Y.S. Hu, W. Sigle, J. Maier, Adv. Mater. 19 (2007) 2087–2091.
[33] C. Li, E.T. Thostenson, T.W. Chou, Compos. Sci. Technol. 68 (2008) 1445–1452.
[34] W. Zheng, S.C. Wong, Compos. Sci. Technol. 63 (2003) 225–235.
[35] W.M. Zhang, X.L. Wu, J.S. Hu, Y.G. Guo, L.J. Wan, Adv. Funct. Mater. 18 (2008) 3941–3946.
[36] S.A. Needham, G.X. Wang, K. Konstantinov, Y. Tournayre, Z. Lao, H.K. Liu, Electrochem. Solid-State Lett. 9 (2006) A315–A319.
[37] G. Derrien, J. Hassoun, S. Panero, B. Scrosati, Adv. Mater. 19 (2007) 2336–2340.
[38] W.M. Zhang, J.S. Hu, Y.G. Guo, S.F. Zheng, L.S. Zhong, W.G. Song, L.J. Wan, Adv. Mater. 20 (2008) 1160–1165.
[39] J. Li, H.K. Dahn, L.J. Krause, D.B. Le, J.R. Dahn, J. Electrochem. Soc. 155 (2008) A812–816.
[40] Q. Cao, H.P. Zhang, G.J. Wang, Q. Xia, Y.P. Wu, H.Q. Wu, Electrochem. Commun. 9 (2007) 1228–1232.
[41] O. Garcia-Zarco, S.E. Rodil, M.A. Camacho-López, Thin Solid Films 518 (2009) 1493.
[42] S.H. Ng, J. Wang, D. Wexler, S.Y. Chew, H.K. Liu, J. Phys. Chem. C 111 (2007) 11131–11138.
[43] D. Larcher, C. Masquelier, D. Bonnin, Y. Chabre, V. Masson, J.B. Leriche, J.M. Tarascon, J. Electrochem. Soc. 150 (2003) A133–A139.
[44] J. Jamnik, J. Maier, Phys. Chem. Chem. Phys. 5 (2003) 5215–5220.
[45] J. Morales, L. Sanchez, F. Martin, F. Berry, X.L. Ren, J. Electrochem. Soc. 152 (2005) A1748–A1754.
[46] L.Q. Mai, B. Hu, W. Chen, Y.Y. Qi, C.S. Lao, R.S. Yang, Y. Dai, Z.L. Wang, Adv. Mater. 19 (2007) 3712–3716.
[47] J. Maier, Nat. Mater. 4 (2005) 805–815.
[48] Y.S. Hu, L. Kienle, Y.G. Guo, J. Maier, Adv. Mater. 18 (2006) 1421–1426.
[49] L.Q. Mai, W. Chen, Q. Xu, J.F. Peng, Q.Y. Zhu, Chem. Phys. Lett. 382 (2003) 307–312.
[50] M.F. Hassan, M.M. Rahman, Z.P. Guo, Z.X. Chen, H.K. Liu, Electrochim. Acta 55 (2010) 5006–5013.
[51] L.J. Fu, L.C. Yang, Y. Shi, B. Wang, Y.P. Wu, Micropor. Mesopor. Mater. 117 (2009) 515–518.